INTERFACE

royalsocietypublishing.org/journal/rsif

Research

Cite this article: Zhang Z, Rosakis P, Hou TY, Ravichandran G. 2020 A minimal mechanosensing model predicts keratocyte evolution on flexible substrates. *J. R. Soc. Interface* **17**: 20200175.
http://dx.doi.org/10.1098/rsif.2020.0175

Received: 14 March 2020
Accepted: 7 April 2020

Subject Category:
Life Sciences–Mathematics interface

Subject Areas:
biomathematics, biomechanics

Keywords:
mechanosensing, cellular locomotion, level set method, keratocytes

Author for correspondence:
Phoebus Rosakis
e-mail: rosakis@uoc.gr

Electronic supplementary material is available online at https://doi.org/10.6084/m9.figshare.c.4944945.

THE ROYAL SOCIETY PUBLISHING

A minimal mechanosensing model predicts keratocyte evolution on flexible substrates

Zhiwen Zhang[1], Phoebus Rosakis[2,3], Thomas Y. Hou[4] and Guruswami Ravichandran[5]

[1]Department of Mathematics, The University of Hong Kong, Pokfulam Road, Hong Kong SAR
[2]Department of Mathematics and Applied Mathematics, University of Crete, Heraklion 70013 Crete, Greece
[3]Institute of Applied and Computational Mathematics, Foundation for Research and Technology-Hellas, Voutes 70013 Crete, Greece
[4]Computing and Mathematical Sciences, and [5]Division of Engineering and Applied Science, California Institute of Technology, Pasadena, CA 91125, USA

PR, 0000-0002-0383-0961

A mathematical model is proposed for shape evolution and locomotion of fish epidermal keratocytes on elastic substrates. The model is based on mechanosensing concepts: cells apply contractile forces onto the elastic substrate, while cell shape evolution depends locally on the substrate stress generated by themselves or external mechanical stimuli acting on the substrate. We use the level set method to study the behaviour of the model numerically, and predict a number of distinct phenomena observed in experiments, such as (i) symmetry breaking from the stationary centrosymmetric to the well-known steadily propagating crescent shape, (ii) asymmetric bipedal oscillations and travelling waves in the lamellipodium leading edge, (iii) response to remote mechanical stress externally applied to the substrate (tensotaxis) and (iv) changing direction of motion towards an interface with a rigid substrate (durotaxis).

1. Introduction

It has long been known that various types of biological cells exert forces that substantially deform their surroundings, such as the elastic substrate they crawl on, or the extracellular matrix they are embedded in [1–4]. It is also recognized that cells sense deformations or stresses that they themselves generate [5,6], or that are caused by external factors, and that they also sense the stiffness of the substrate [7]. These activities are known as mechanosensing (see [8], for a review), and they facilitate some important modes of cell migration or evolution: tensotaxis [9], the movement or protrusion towards regions of higher tensile stress, and durotaxis [10], the tendency to move towards regions of higher stiffness. These processes play a key role in wound healing, fibrosis, tumour formation and cancer metastasis [11]. Mechanosensing has been studied in the context of shape regulation and multi-cell interactions [5,12–15].

The cells whose mechanosensing behaviour has been studied the most are fibroblasts [1,10,16]. More recently, it was determined that fish epidermal keratocytes also exert strong contractile forces on their elastic surroundings, to the extent that they can cause a sufficiently thin and compliant elastic substrate to wrinkle [3]. Keratocytes are well known for their persistent, high-speed, steady locomotion while maintaining a characteristic crescent-like shape that is quite different from their stationary round configuration, e.g. [17,18]. Because of this, they have served as a model system for the study of cell locomotion on substrates of various types, through experiments [3,18–20] and theoretical modelling [21–26].

Theoretical models of keratocyte locomotion have largely focused on detailed biophysical and biochemical processes within the cell, governing spatial concentrations of constituents such as actin, myosin and adhesion complexes [23,24], but have rarely considered mechanosensing [25–27].

Here, we adopt an alternative approach: we propose a mathematical model for the evolution of keratocytes on elastic substrates that is entirely based on hypotheses of active mechanosensing. The model is intentionally minimal in describing processes within the cell, focusing instead on purely mechanical interaction of the lamellipodium with the substrate, through active force generation, passive stress detection and active response to stress sensing via local shape evolution. The proposed mechanism of cell evolution is a feedback loop: the lamellipodium applies tractions onto the elastic substrate; the resulting stress field in the substrate depends on the instantaneous shape of the cell, while the evolution of the cell shape depends on the substrate stress, closing the feedback loop. The new hypothesis we make is that the shape of the cell evolves according to a local evolution law. Specifically, at each point on the lamellipodium boundary, the normal boundary velocity is determined by the local stress state of the substrate, in a way that favours local protrusion under tension and retraction under compression.

We model the substrate as a linear elastic thin sheet in a state of plane stress [28], as in experiments on compliant silicone sheets [3,29,30] that facilitated visualization of substrate deformation caused by keratocyte-applied tractions.

We assume a centripetal retrograde velocity field in the lamellipodium, representing actin flow. While appropriate for static keratocytes [18], which are round in shape, this assumption is less accurate for locomoting keratocytes [18]. In accordance with experimental observations [18,31], we thus include a generalization, where the velocity field is polarized in the direction of motion.

Tractions applied onto the substrate by the cell are assumed proportional to the actin velocity field relative to the substrate. This results in a stress field that is determined by the shape of the lamellipodium through elastic equilibrium. The motion of the lamellipodium boundary is determined by a competition between retrograde actin velocity and the actin polymerization speed normal to the boundary. We assume that at each boundary point, this speed is equal to a function of the component of the substrate stress normal to the lamellipodium boundary. While the structural mechanism behind this is not clear, we note that actin fibres are known to act as tension sensors [7,32–34], while formins control actin polymerization rate in a mechanosensitive, tension-dependent way [35], affected by external mechanical disturbances [36]. This could point towards a link between polymerization speed and substrate tension. For an alternative viewpoint, see [37].

Given the shape of the lamellipodium, the normal velocity of its boundary is determined at each point. This determines the evolution of the lamellipodium shape through a Hamilton–Jacobi equation, coupled to the elastic equilibrium equation. The resulting mathematical problem is amenable to numerical simulation via the level set method [38–40] which has been applied to cell evolution [23,41]. In addition to the substrate stress field, the evolving shape of the lamellipodium is the main output of the model.

Despite its simplicity, the model predicts multiple different modes of locomotion behaviour, owing to its rich bifurcation response. These include symmetry breaking from the stationary centrosymmetric to the well-known steadily propagating crescent shape as observed [18]. We show how mechanosensitive coupling between cell shape evolution and substrate stress acts as a feedback loop to bring about the symmetry breaking necessary for locomotion. Asymmetric bipedal oscillations seen in experiments [42] and travelling waves in the lamellipodium leading edge [31,43] occur in model simulations. These results suggest that the mechanism here is further symmetry breaking caused by actin flow polarization. In addition, simulated cells exhibit tensotaxis, or motion towards mechanical tension externally applied to the substrate (seen in human keratinocytes [44]), and away from compression, as observed in lamellipodium fragments without a nucleus [17]. The model also exhibits durotaxis, or turning towards an interface with a rigid substrate as observed in various locomoting cells [45].

2. Methods

We model fish epidermal keratocytes crawling on a thin deformable planar substrate. We assume that the latter is composed of linear elastic homogeneous isotropic material undergoing small in-plane deformations. The linear theory of elasticity is used; out-of-plane displacements are neglected, while all forces are assumed to act in the plane. As in [29], we assume plane stress for the substrate, which allows us to reduce the description to that of a two-dimensional (2D) medium that occupies the entire plane [28]; see plane stress in electronic supplementary material. The time-dependent displacement vector field is $\boldsymbol{u} = \boldsymbol{u}(\boldsymbol{x}, t)$, where $\boldsymbol{x}$ is position vector in the plane and t is time. The 2D stress tensor (thickness resultant of the 3D stress, i.e. electronic supplementary material, eqn (2)) is related to the thickness-averaged, in-plane displacement gradient

$$\boldsymbol{S} = \bar{\lambda}(\nabla \cdot \boldsymbol{u})\boldsymbol{I} + \bar{\mu}(\nabla \boldsymbol{u} + \nabla \boldsymbol{u}^T), \tag{2.1}$$

in the isotropic case considered here, where $\bar{\lambda} > 0$ and $\bar{\mu} > 0$ are the surface-Lamé constants (see plane stress in electronic supplementary material) and $\boldsymbol{I}$ the identity tensor.

The cell is modelled as a time-dependent region Ω_t in the plane. The cell interacts with the substrate by exerting forces on it. This occurs mostly in the lamellipodium, while the part of the cell body around and under the nucleus need not even be in contact with the substrate [20]. Accordingly, Ω_t represents the lamellipodium only. Forces exerted by the lamellipodium onto the substrate are assumed to be in-plane; they are due to retrograde actin flow within the cell caused by myosin contraction pulling at radial actin fibres; e.g. [18]. The actin exerts a force onto the substrate through drag and/or adherence to focal adhesions that are attached to it [46]. For stationary cells, there is evidence [18,47,48] that the actin network within the cell arranges itself radially from the centroid of the cell and exerts centripetal tractions onto the substrate [3]. For fibroblasts on elastic substrates, this occurs independently of shape [48]. Stationary keratocytes assume a disk shape; the lamellipodium is approximately an annulus surrounding the nucleus. The direction of the actin flow velocity is radially inward towards the cell centre [18] and the magnitude increases with distance from the centroid.

We generalize this for moving cells. We assume that the actin velocity relative to the substrate is radially inward towards a point $\boldsymbol{x}_0(t)$ travelling with the cell, and its magnitude increases linearly with distance from $\boldsymbol{x}_0(t)$. Thus the actin velocity in the substrate frame is

$$\boldsymbol{v}_s(\boldsymbol{x}, t) = -\gamma(\boldsymbol{x} - \boldsymbol{x}_0(t)),$$

for $\boldsymbol{x}$ in Ω_t, where the actin velocity coefficient $\gamma > 0$ is a constant.

In the cytoskeleton, myosin motors contract the actin fibres and pull them backwards towards the nucleus and perinuclear region. This retrograde flow causes actin to drag against the adhesion complexes, inducing a frictional drag force against the substrate, which is frequently modelled as a viscous drag force [23,31,49]. We follow this approach here and model the traction

exerted onto the substrate by the keratocyte lamellipodium (due to viscous actin dragging against the substrate) as a viscous drag force per unit area $\boldsymbol{b} = \zeta \boldsymbol{v}_s$, where $\zeta > 0$ is a drag coefficient. The drag coefficient ζ is taken to be a constant, as in [31,49]. This means we assume a spatially uniform adhesion strength. This is more justifiable for keratocytes studied here, compared to fibroblasts. Focal adhesions are discrete and strong in fibroblasts [50], causing corners in their shape and restrictions to mobility, but much weaker, diffuse and uniform in keratocytes (smooth shape, fast uniform motion). To quote [51] 'perhaps the main reason for the different shape of keratocytes and fibroblasts is the nature of adhesions in these cells. In keratocytes, discrete strong adhesions play a minor role, whereas in fibroblasts their role is significant, disrupting the coherent protrusion of the actin network.' In view of this, we assume a uniform adhesion strength, leading to a constant drag coefficient ζ [23,49]. As a result the drag force per unit area is

$$\boldsymbol{b}(\boldsymbol{x}, t) = -K\chi_{\Omega_t}(\boldsymbol{x})(\boldsymbol{x} - \boldsymbol{x}_0(t)), \tag{2.2}$$

where $K = \gamma\zeta$ and $\chi_{\Omega_t}(\boldsymbol{x}) = 1$ for $\boldsymbol{x}$ in Ω_t and 0 outside Ω_t is the characteristic function of Ω_t.

The total external traction force per unit area acting on the cell is $-\boldsymbol{b}(\boldsymbol{x}, t)$, the reaction exerted by the substrate. Both cell locomotion speeds and actin flow speeds are typically less than 0.5 $\mu m\, s^{-1}$, whereas elastic wavespeeds of some of the softest substrates used in experiments can be estimated to be of the order of metres per second from modulus measurements [30]. In addition, within the cell inertia effects are negligible compared to viscous forces, with the extremely small Reynolds numbers prevalent in cell biology [22]. Therefore, the process is essentially quasi-static both for the substrate and the cell, and equilibrium is assumed to hold. The total force acting on the cell must vanish, namely

$$\int_{\Omega_t} \boldsymbol{b}(\boldsymbol{x}, t)\, \mathrm{d}\boldsymbol{x} = \boldsymbol{0}. \tag{2.3}$$

In view of (2.2), this dictates that $\boldsymbol{x}_0 = \bar{\boldsymbol{x}}$, the cell centroid, given by

$$\bar{\boldsymbol{x}} = \bar{\boldsymbol{x}}(t) = \frac{\int_{\Omega_t} \boldsymbol{x}\, \mathrm{d}\boldsymbol{x}}{\int_{\Omega_t} \mathrm{d}\boldsymbol{x}}, \tag{2.4}$$

as first observed in [47]. This implies

$$\boldsymbol{v}_s(\boldsymbol{x}, t) = -\gamma(\boldsymbol{x} - \bar{\boldsymbol{x}}), \tag{2.5}$$

so that

$$\boldsymbol{b}(\boldsymbol{x}, t) = -K\chi_{\Omega_t}(\boldsymbol{x})(\boldsymbol{x} - \bar{\boldsymbol{x}}(t)) = \zeta \boldsymbol{v}_s(\boldsymbol{x}, t). \tag{2.6}$$

A generalization of (2.6) is motivated by observations [18,31] of the actin velocity field of locomoting keratocytes, which loses radial symmetry and becomes polarized in the direction of cell motion [18]. We include this variation of actin velocity in our model in a phenomenological yet minimal form. We assume that at a given distance from the centroid, the actin velocity in the cell frame is more pronounced in the direction of motion than in the perpendicular direction, by a factor depending on the cell centroid velocity $\bar{\boldsymbol{v}} = \dot{\bar{\boldsymbol{x}}}$. We still assume that $\boldsymbol{v}_s$ is linear in $\boldsymbol{x} - \boldsymbol{x}_0$, but with magnitude that is larger in the direction $\bar{\boldsymbol{v}}$ of cell motion

$$\boldsymbol{v}_s = -\gamma(\boldsymbol{I} + e\bar{\boldsymbol{v}} \otimes \bar{\boldsymbol{v}})(\boldsymbol{x} - \boldsymbol{x}_0), \tag{2.7}$$

where the actin velocity coefficient $\gamma > 0$ and polarization coefficient $e \geq 0$ are constants. In a basis with vectors along, and normal to, the direction of cell motion, the matrix $\boldsymbol{I} + e\bar{\boldsymbol{v}} \otimes \bar{\boldsymbol{v}}$ takes the form

$$\boldsymbol{I} + e\bar{\boldsymbol{v}} \otimes \bar{\boldsymbol{v}} = \begin{pmatrix} 1 + e|\bar{\boldsymbol{v}}|^2 & 0 \\ 0 & 1 \end{pmatrix}.$$

Thus the velocity component along the direction of cell motion is amplified by a factor $1 + e|\bar{\boldsymbol{v}}|^2$ compared to the radially symmetric actin velocity field. When $\bar{\boldsymbol{v}} = \boldsymbol{0}$, or for the choice $e = 0$, the velocity field (2.7) reduces to the radially symmetric one, (2.5). Cell equilibrium (2.3) with $\boldsymbol{b} = \zeta \boldsymbol{v}_s$ and $\boldsymbol{v}_s$ given by (2.7) determines

$$\boldsymbol{b}(\boldsymbol{x}, t) = -\chi_{\Omega_t}(\boldsymbol{x})K(\boldsymbol{I} + e\bar{\boldsymbol{v}} \otimes \bar{\boldsymbol{v}})(\boldsymbol{x} - \bar{\boldsymbol{x}}). \tag{2.8}$$

The substrate experiences an in-plane traction force (per unit substrate area) equal to $\boldsymbol{b}(\boldsymbol{x}, t)$ on its top surface, representing tractions exerted by another body (the cell) in contact with it. Assuming plane stress conditions [28] and performing a standard thickness average of the three-dimensional equilibrium equations (see plane stress in electronic supplementary material) for the substrate, we find,

$$\nabla \cdot \boldsymbol{S}(\boldsymbol{x}, t) + \boldsymbol{b}(\boldsymbol{x}, t) = \boldsymbol{0}, \tag{2.9}$$

Here, $\boldsymbol{S}$ is the two-dimensional stress (i.e. electronic supplementary material, eqn (2)) acting in the plane of the substrate. It is related to the thickness-averaged substrate displacement via (2.1), while $\boldsymbol{b}$ is traction force per unit area exerted by the cell onto the substrate and h is the substrate thickness.

A central ingredient of our model is the evolution law that governs the motion of the lamellipodium boundary curve C_t. It is based on the notion that cells can detect stress in the substrate (mechanosensing) [32] and make local adjustments to their shape accordingly.

In order to characterize the moving curve C_t, it suffices to specify its normal velocity $V_n(\boldsymbol{x}, t)$ at each $\boldsymbol{x} \in C_t$ and time t. To begin with, we follow previous models [22,26,52] in assuming

$$V_n = \boldsymbol{v}_s \cdot \boldsymbol{n} + v_p \quad \text{on } C_t. \tag{2.10}$$

Here, it is assumed that actin filaments polymerize at the boundary with outward normal speed v_p but also flow inwards with velocity $\boldsymbol{v}_s$ whose normal component is $\boldsymbol{v}_s \cdot \boldsymbol{n}$. Thus the net normal boundary velocity V_n is the excess of the polymerization speed v_p over the retrograde inward actin flow speed in the direction normal to the cell boundary. It remains to characterize the polymerization speed v_p. A point of departure from other models of keratocyte evolution [21–26] is the incorporation of mechanosensing in a constitutive relation for v_p. In particular, we hypothesize that the actin polymerization speed depends on the substrate stress.

In order to identify a possible structural mechanism behind this hypothesis, we observe that actin fibres are known to act as tension sensors [7,32,33]; also cyclic variations in the assembly/disassembly rate of actin are synchronous to traction fluctuations at focal adhesions [34]. A more direct link between polymerization speed and substrate tension may be provided by formins, proteins that play a major role in actin polymerization. Experiments have shown that formins control the polymerization rate of the actin filaments in a mechanosensitive manner, i.e. the polymerization rate depends increasingly on the local state of tension force [35]. In addition, mechanical forces exerted onto the cell membrane, or stretching the substrate, affected formin-controlled polymerization rate [36]. Through cell-substrate adhesions, substrate stress is transmitted to the lamellipodium membrane, while formins anchor the barbed ends of actin filaments to the membrane [33] at the leading edge. Substrate stress in the vicinity of the leading edge is thus likely to affect the polymerization rate through mechanosensitive formins, providing plausibility to the mechanism proposed here.

In previous models, the polymerization speed v_p is sometimes assumed to be constant [52], or a function of one of the concentrations within the cell, for example G-actin or myosin [23]. Here, we follow a different approach and link polymerization speed to substrate stress. We include two contributions:

$$v_p = G(\boldsymbol{n} \cdot \boldsymbol{S}\boldsymbol{n}) + \Lambda\left(1 - \frac{A(t)}{A(0)}\right) \quad \text{on } C_t. \tag{2.11}$$

The rationale behind the first term in (2.11) is as follows. We make a mechanosensing hypothesis, which we refer to as local

tensotaxis: the lamellipodium boundary tends to protrude locally in areas of tension and recede in areas of compression. This is motivated by a global tensotaxis behaviour: cells are known to move away from regions of compressive stress [53], in addition to favouring tensile stress [10]. Since stress $\boldsymbol{S}$, being a tensor, can be both compressive and tensile at the same point (in different directions) we must clarify the precise meaning of tension and compression. On an isotropic substrate, there are no other special directions, except the lamellipodium boundary unit normal $\boldsymbol{n}$. It is thus reasonable to choose the component of stress in this normal direction, $\boldsymbol{n}\cdot\boldsymbol{S}\boldsymbol{n}$, as the one related to the polymerization rate. An obvious choice would be a linear relation between normal polymerization velocity and normal tension, however, we require the velocity to remain bounded as cells seem to move with bounded speeds on substrates, rarely exceeding a few micrometres per second, so it is reasonable to assume instead a relation that saturates for large values of tension. Thus in (2.11), we choose

$$G(z) = \beta\frac{z}{\sigma_0 + |z|}, \tag{2.12}$$

which is an odd, increasing function that remains bounded for large values of its argument, with β a positive mobility coefficient and σ_0 a constant with dimensions of stress. Accordingly, apart from the second term in (2.11), v_p changes signs depending on whether the normal stress component $\boldsymbol{n}\cdot\boldsymbol{S}\boldsymbol{n}$ is tensile or compressive.

The second term in (2.11) is a penalty term that tends to maintain the area $A(t)$ of Ω_t constant (Λ =const. > 0). Here, we follow common practice in enforcing essentially constant area [23,26,31]. This is supported by experiments; Keren *et al.* [21] found that 'projected cell area, although quite variable across the [cell] population, was essentially constant for a given cell (fig. 2a in [21]). This suggests that the area, probably determined by the total amount of available plasma membrane or by tight regulation of the membrane surface area, is intrinsic to each cell and constant through time.'

Once an initial lamellipodium shape Ω_0 at $t = 0$ is specified, further evolution is governed by the normal velocity V_n, (2.10), where v_p is given by (2.11), v_s is determined by (2.7), and the stress $\boldsymbol{S}$ is obtained from the solution of equations (2.9), (2.1), with forcing given by the cell traction force $\boldsymbol{b}$ from (2.8).

We use the level set method [38–40] which has been successfully applied to cell evolution study, e.g. [23,41] to solve for the evolution of the lamellipodium boundary C_t together with the other model equations. The *level set function* $\varphi(\boldsymbol{x}, t)$ vanishes on C_t, is positive inside Ω_t and negative outside it. It evolves according to the *level set equation*

$$\varphi_t + V_n|\nabla\varphi| = 0, \tag{2.13}$$

with V_n the normal velocity of C_t, which is determined by the equation $\varphi = 0$. The model thus comprises equations (2.9), (2.13), with $\boldsymbol{b}$ given by (2.8), V_n supplied by equations (2.10), (2.11).

2.1.1. Non-dimensional form and parameter estimation

The model involves eight constitutive parameters. The substrate is characterized by the Lamé constants $\lambda > 0$ and $\mu > 0$, while the cell by the kinetic coefficient β, actin velocity coefficient γ, drag coefficient ζ, velocity polarization e, area penalty coefficient Λ and stress coefficient σ_0. We define the non-dimensional variables

$$\tilde{\boldsymbol{x}} = \frac{\gamma}{\beta}\boldsymbol{x}, \quad \tilde{t} = \gamma t, \quad \tilde{v} = \frac{v}{\beta}, \quad \tilde{\boldsymbol{S}} = \frac{1}{\sigma_0}\boldsymbol{S}$$

This shows that γ is in essence a time scale, while β sets a velocity scale. We also define the non-dimensional constants

$$\tilde{\zeta} = \frac{\beta^2}{\gamma\sigma_0}\zeta, \quad \tilde{e} = \beta^2 e, \quad \tilde{\Lambda} = \frac{\Lambda}{\beta}.$$

We then revert to the same notation (without tilde) for the non-dimensional variables and constants; this is equivalent to setting $\beta = 1$, $\gamma = 1$, $\sigma_0 = 1$ in the original system. The remaining independent parameters for the cell are ζ, e, Λ. Since the forcing term (2.8) is independent of the Lamé moduli λ, μ, for null displacement or traction-free boundary conditions, a theorem of linear elasticity [54] asserts that the thickness resultant stress field $\boldsymbol{S}$ depends on λ, μ only through their ratio, or equivalently Poisson ratio $\nu = \frac{\lambda}{2(\lambda+\mu)}$. Thus there is one independent non-dimensional parameter ν for the substrate, or a total of four non-dimensional model parameters. Unless otherwise specified, in our simulations, we used a standard parameter set of

$$\beta = 2.5\,L/T, \quad \gamma = 0.8/T, \quad K = \gamma\zeta = 3F/L,$$
$$e = 2(T/L)^2, \quad \Lambda = 30L/T \quad \text{and} \quad \nu = 1/4. \tag{2.14}$$

Here, L, T and F are computational units of length, time, and traction (force per unit area), respectively, or scale factors relating computational to physical parameter magnitudes. We choose $L = 5$ µm and $T = 15$ s. This gives rise to moving cell size of roughly $20 - 40$ µm and typical steady cell locomotion speed $0.2\ \mu\text{m s}^{-1}$ from our simulations. These agree with reported values [18,21]. Then the choice $\gamma = 0.8/T = 0.05\ \text{s}^{-1}$ yields actin velocity magnitudes $\gamma L = 0.25\ \mu\text{m s}^{-1}$ of the observed order [18,22]. Letting the traction (force per unit area) scale be $F = 100\ \text{pN}\,\mu\text{m}^{-2}$ [19], the choice $K = 3F/L$ yields average tractions $KL = 300\ \text{pN}\,\mu\text{m}^{-2} = 3000\ \text{dyn cm}^{-2}$ within the experimentally measured range [19,30]. Also for these values we obtain a drag coefficient $\zeta = K/\gamma = 1200\ \text{pN s}\,\mu\text{m}^{-3}$, close to the estimate of $1000\ \text{pN s}\,\mu\text{m}^{-3}$ of [22]. The parameter Λ is not easy to estimate, but results are not very sensitive to its value. The polarization coefficient has the standard value $e = 18\ \text{s}^2\,\mu\text{m}^{-2}$. Equation (2.7) allows an estimate of the difference of actin speed magnitude between the front and the wings (furthest from the x-axis of motion) of $\gamma e V^2 L$ with V the cell speed. From low adhesion strength data of [31], we obtain roughly $e = 12\ \text{s}^2\,\mu\text{m}^{-2}$ or two-thirds the standard value used here. In physical, units model parameters are

$$\beta = 0.83\ \mu\text{m s}^{-1}, \quad \gamma = 0.05\,\text{s}^{-1}, \quad K = 60\ \text{pN}\,\mu\text{m}^{-3},$$
$$e = 18\ \text{s}^2\,\text{m}^{-2}, \quad \Lambda = 10\ \mu\text{m s}^{-1} \quad \text{and} \quad \nu = 1/4. \tag{2.15}$$

In general, our standard parameter values are consistent with estimates from experiments.

3. Results and discussion

3.1.1. Symmetry breaking and topological transition

Keratocytes typically assume a roughly circular shape when stationary, with an annular lamellipodium surrounding the nucleus [18]. Contact and force transmission with the substrate occurs only at the lamellipodium and not the nucleus and organelles [20]. Accordingly, we choose the initial lamellipodium region Ω_0 to be an annulus in the centre of the square domain D, with the nucleus excluded from description by the model. We find that for standard parameters (2.15), an annulus with radii 8.5 µm and 17 µm and lamellipodium area $680\ \mu\text{m}^2$ remains stable and radially symmetric during our computations. These values are comparable with the ones in [18] fig. 2a. The actin velocity field in the annulus is centripetal. Next, we modify the annulus Ω_0 with a slight shape imperfection, in the form of a localized slight thinning or dimple at the left side of the cell (figure 1*a*). We try different perturbations in the form of indentations of different depth and width on one side of the annulus. We find that either the cell returns to the initial radially symmetric state if the perturbation is small, or a sufficiently large

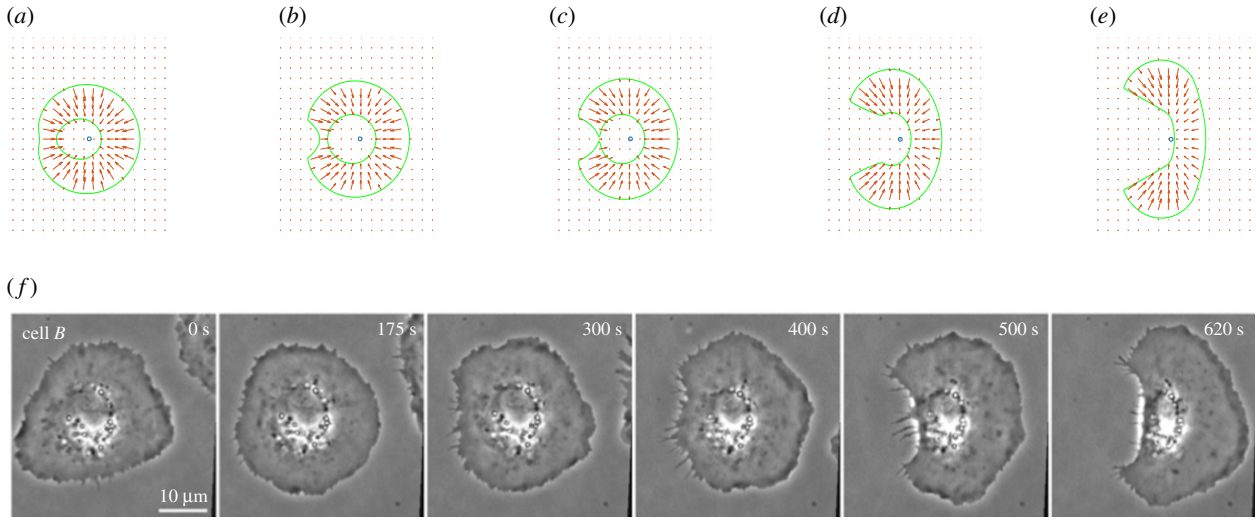

Figure 1. Transition from the stationary annulus configuration to the locomoting crescent shape of the keratocyte lamellipodium, from our model simulation with standard parameters (2.15): (*a*) initial condition for model simulation: stationary annular lamellipodium with centripetal velocity field and imperfection, (*b*) retraction (pinching) of the left side, (*c*) topological transition, (*d*) motile horseshoe shape, (*e*) fully developed locomoting crescent shape; motion is to the right and (*f*) image sequence of observed transition from [18].

indentation grows and breaks the symmetry. This causes the lamellipodium outside the boundary to move towards the centre in the vicinity of the imperfection (figure 1*b*). The localized retraction causes further thinning until the lamellipodium pinches off completely and a topological transition occurs (figure 1*c*) as the annulus splits off into a simply connected, horseshoe-shaped domain (figure 1*d*). The topological change is evident as a result of excluding the nucleus from Ω_t. Retraction of the cell rear occurs before the front starts to protrude, as reported in the experiments of [18]. The horseshoe flattens into a banana or crescent shape which only has symmetry about the x-axis. This polarized shape starts moving in the positive x-direction and quickly reaches steady shape and velocity, which it maintains for a long time (figure 1*e*). The transition from the annular stationary state, to the polarized, crescent-shaped, locomoting state is remarkably similar to the sequence of observations reported in ([18], fig. 2a); an example is reproduced here in figure 1*f*. The locomoting state is independent of the shape of the perturbing dimple, provided the latter is severe enough to cause symmetry breaking. The locomoting crescent is thus a stable travelling state.

We find that the initial transition from static annulus to locomoting crescent is not strongly dependent of parameters, because the centroid velocity is small, hence the polarization term does not play an important role. In the absence of polarization ($e = 0$) the actin velocity (2.5) is radially symmetric, so it is the lamellipodium that breaks radial symmetry during the transition.

Mechanosensitive coupling between cell shape evolution and substrate stress acts as a feedback loop to bring about the symmetry breaking necessary for locomotion. Perturbing the radial symmetry of the static cell shape breaks the symmetry of the substrate stress field; this induces asymmetry of the polymerization velocity (protrusion rate), which in turn amplifies asymmetric polarized shape evolution, closing the feedback loop, even in the presence of a radial, non-polar actin flow. In the presence of polarization ($e > 0$), the radial symmetry of the velocity field is broken as well, once the centroid moves; thus the presence of polarization affects the long-term locomoting shape of the lamellipodium.

3.1.2. Steady motion and parameter dependence

Consistent with the observations of [18], our model predicts that following symmetry breaking, topological change, and flattening of the broken annulus into a crescent, the cell settles into steady motion at essentially constant shape and velocity in the low polarization regime $e < 2$, $K < 15$. An example of full transition from static annulus to fully developed steady state can be seen in electronic supplementary material, video SV1 (standard parameters except for $e = 1.5$). The long-time fully developed crescent shape depends on the parameters K and e. Figure 2 shows the fully developed crescent shape for various combinations of K and e in the low polarization regime. In particular, for fixed K, the aspect ratio increases with increasing e, while for fixed e, raising K increases the length of the trailing horns and the overall diameter slightly, but decreases the aspect ratio. The reasons for this dependence stem from (2.10). The forcing term $\boldsymbol{b}$ in (2.9), and hence the stress field, is proportional to K. The stress in turn controls the size of the term v_p in (2.10). At the sides of the cell furthest away from the axis of motion, V_n vanishes, so an increase in v_p for larger K must be balanced by an increase in absolute value of v_s at the sides, which can only occur by increasing the diameter of the cell, as v_s depends on distance from the centre. An increase in e polarizes both the actin velocity and the forcing, hence the stress, and the entire right-hand side of (2.10), in the direction of motion, hence the normal direction $\boldsymbol{n}$ is likely to be closer to the motion direction as well. This causes a flatter crescent, whose aspect ratio must be larger than a rounded one, due to the area constraint. More drastic increases in polarization e have more profound effects on motion, considered in detail in the next section.

See [3,20,21] for various examples of steady shapes of different aspect ratios but similar overall form. The crescent-shaped lamellipodium and persistent, steady motion are

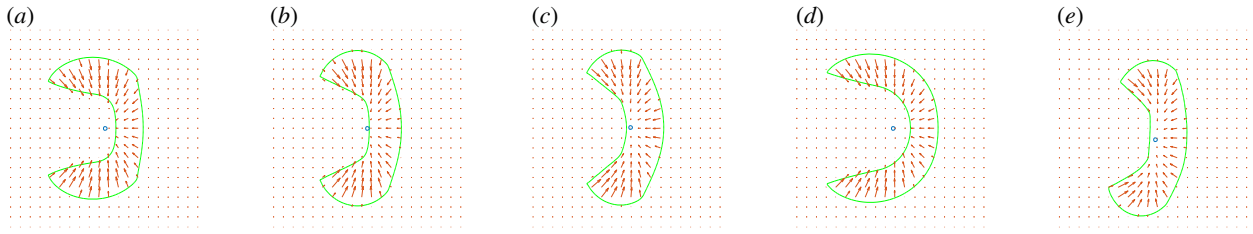

Figure 2. Parameter dependence of fully developed locomoting crescent lamellipodium shape in the low actin velocity polarization regime. Motile keratocyte moving to the right. (*a–c*) $K = 3$ and $e = 0$, 1.5, 2, respectively. (*d*,*e*) $K = 10$ and $e = 0$, 2, respectively. Green curve is lamellipodium shape, actin velocity vectors are shown red.

well-known characteristics of crawling keratocytes [18,22], not only whole cells but also separated fragments of the lamellipodium [17,52] without the nucleus. This is also predicted by our model; see the Tensotaxis section below.

3.1.3. Bipedal oscillations and lamellipodial travelling waves

Henceforth, we fix $K = 3$ and focus on the effect of varying the polarization coefficient e. We find that there are roughly three regimes of locomotion, depending on its value. For low polarization, approximately $0 \leq e < 2$, following the transition from annular stationary to locomoting crescent shape, propagation quickly becomes steady with constant velocity and no shape change, as described above.

In the intermediate polarization regime (roughly $2 \leq e \leq 4$), after settling to steady motion, the cell suddenly switches to oscillatory propagation. The centroid follows a roughly sinusoidal trajectory that oscillates about the x-axis, with the onset of oscillations at $e = 2$ (figure 3*a*), and higher amplitude as e increases, e.g. $e = 3$ (figure 3*b*). Hence the direction of polarization, which is along the centroid velocity vector in our model, oscillates about the x direction as well. The substrate displacements alternate from nearly symmetric to antisymmetric with respect to the x-axis twice over an oscillation period (red arrows in figure 4*a–d* and electronic supplementary material, video SV2). The lamellipodium oscillates somewhat rigidly with little shape change, except at the posterior trailing edges, which alternate from a pointed to a rounded shape out of phase with each other (see lamellipodium contours in figure 4*f* and *a–d*). The bipedal nature of these oscillations is illustrated (figure 5) by tracking the two trailing points on the lamellipodium boundary, or points with the smallest x-coordinate on the lamellipodium boundary above and below the x-axis. Their trajectories, x-coordinates and x-velocities undergo antiphase oscillations as shown in figure 5. The trailing points not only oscillate out of phase with each other; they even undergo alternating intermittent backward motion.

Thus the cell propagates through asymmetric bipedal motion, as shown in electronic supplementary material, video SV2; see also video SV3. These qualitative characteristics occur in keratocyte motion reported in [42], where it is noted that 'in persistently polarized, fan-shaped cells, retraction of the trailing edge on one side of the cell body is out of phase with retraction on the other side, resulting in periodic lateral oscillation of the cell body'. A comparison of electronic supplementary material, video SV2 and ([42] electronic supplementary material, movie S2) shows very similar alternating trailing edge retraction shapes (alternate rounded and pointed) but a larger wavelength in the latter.

Increasing e decreases the oscillation frequency and the cell speed, figure 3*e*, which correlate with each other, figure 3*f* , in accordance with [42]. This agreement is qualitative; the spatial wavelength of centroid oscillation in our simulations seems much smaller than the ones reported in [42]. Choosing computational units to match cell size and speed reported in [42] (x-unit = 5 µm and t-unit = 15 s in figure 5*d–f*) predicts an oscillation frequency of $\omega = 0.7\ \mathrm{s}^{-1}$, roughly three times that reported in fig. 1, [42]. The overall centroid trajectory (with oscillations averaged out) becomes curved and gradually strays away from the x-axis more for higher values of e, figure 3*d*. This is also observed in locomoting keratocytes [42].

The high polarization regime ($e \geq 5$) is characterized by increasingly severe, more irregular lamellipodium shape distortions, in phase with centroid oscillations that are superposed on a trajectory curving further away from the x-axis for higher values of e, figure 3*c*,*d* and 4*f –i*. A striking feature of this regime is the formation of kinks in the anterior lamellipodium front, figure 4*g–k*, which would retain its convexity in lower polarization regimes. Each such kink is the leading edge of a protrusion that propagates along the anterior lamellipodium boundary, away from the anterior centre, outwards to the sides of the lamellipodium (successive contours in figure 4*j*,*k* and electronic supplementary material, videos SV4 and SV5). Remarkably, these travelling protrusions exhibit qualitative similarities with travelling waves observed on the anterior lamellipodium edge of keratocytes on high adhesion strength substrates [31,43]; an example is shown here in figure 4*l* (reproduced from Fig. 1A in [43]). There are various differences between the travelling protrusions seen in our simulations and reported in [31,43]. In our case, protrusions can be more angular and less prominent than those reported in [43]. In addition trailing lamellipodium edges are more pronounced in our simulations, while anterior profiles are flatter, than those observed. These differences are illustrated by a comparison of figure 4*j*,*k* with 4*l*.

The trajectories of these cells are more erratic and the centroid position oscillations are non-smooth figure 3*d*,*e*, compared to those of the intermediate polarization regime. The centroid oscillation frequency and speed are substantially lower than those of oscillating cells with intermediate polarization, figure 3*e*, in qualitative accord with [31]. On the other hand, our prediction of oscillation frequency for cells travelling with speeds matching those reported in fig. 1*a*, [43] overestimates their oscillation frequency roughly by a factor of 5.

We are confident that the observed oscillations are not an artefact of the numerical method used, but an essential feature of our model's behaviour, as we have confirmed through a numerical convergence study; see electronic supplementary material.

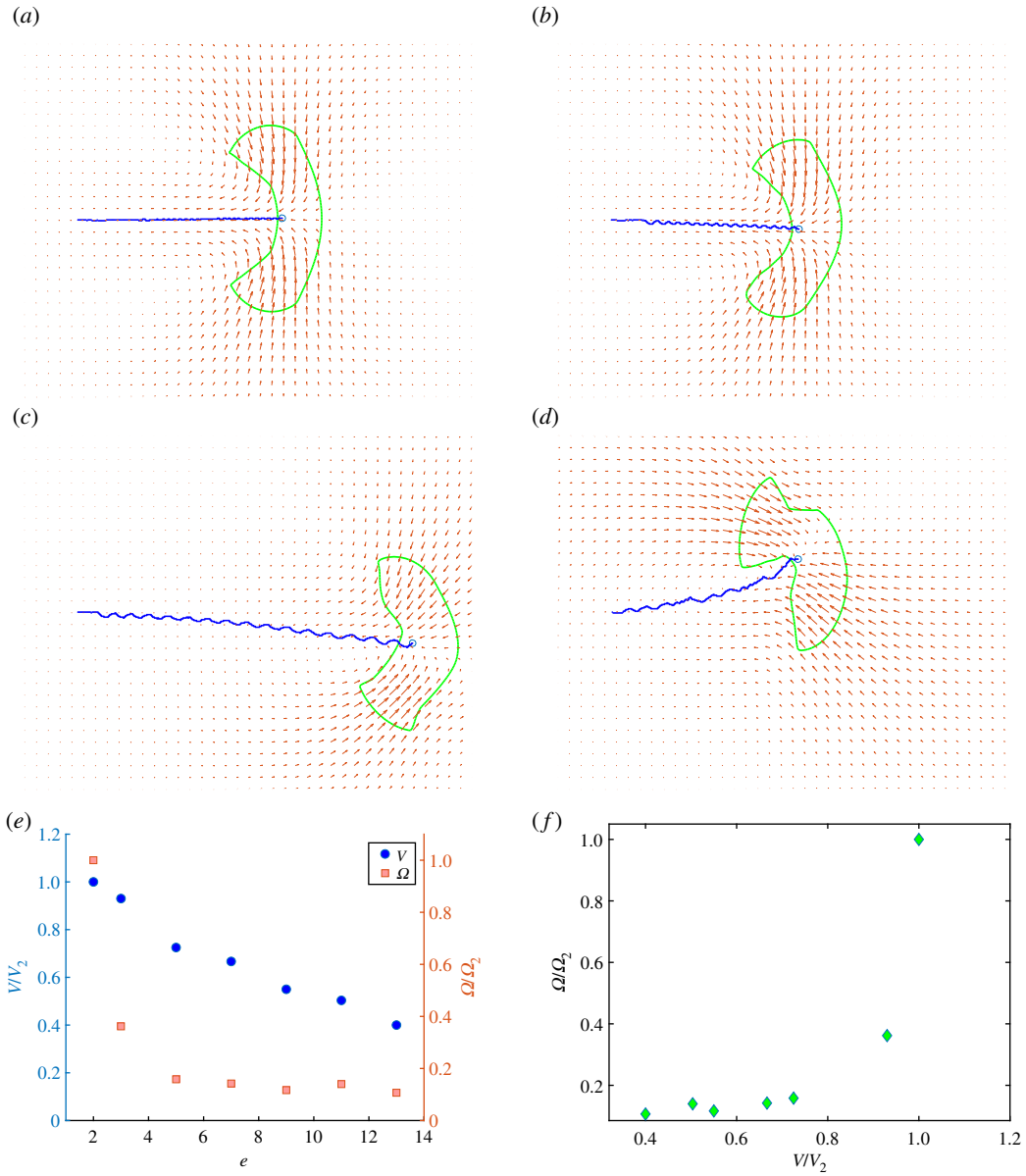

Figure 3. Oscillatory and unsteady motion in the intermediate and high velocity polarization regimes. Blue curve: centroid trajectory with wiggles. Note increasing wavelength, and increasing deviation from the *x*-axis, from (*a*) to (*d*). Green curve: lamellipodium shape. Red arrows: substrate displacements. Here, $K = 3$ in all snapshots. (*a*,*b*) Intermediate polarization regime with bipedal oscillations and $e = 2$, 3, respectively. (*c*,*d*) High polarization regime with irregular oscillations and travelling waves (kinks) on anterior lamellipodium boundary and $e = 5$, 11, respectively. (*e*) Average centroid speed V and frequency Ω versus velocity polarization e from our simulations. Both are normalized by the speed V_2 and frequency Ω_2 from the run with $e = 2$. (*f*) Average frequency Ω correlates with average centroid speed V.

The shift from steady motion to oscillations, as well as the emergence of travelling lamellipodium waves as polarization is increased, seem to be bifurcation phenomena. Our simulations suggest that velocity polarization in the direction of the centroid velocity plays a central role in these non-steady propagation modes. This may happen because a polarized actin velocity field possesses an additional degree of freedom, namely, the direction of polarization; this direction can oscillate, compared to a radial, non-polar velocity field.

Polarization occurs in the direction of cell centroid velocity and introduces an additional degree of freedom. When the centroid undergoes sinusoidal oscillations, the polarization direction oscillates out of phase with the lamellipodium, as can be inferred from figure 5*b*. If the lamellipodium shape were rigid, the stress field would rotate with it and so would the velocity field (which is coupled to the stress field) prohibiting out of phase oscillations. However, additional distortional modes of lamellipodial shape change do allow out of phase deviations between the lamellipodium axis and the polarization direction. Eventually, the rigid rotation mode is likely to provide a restoring tendency for the polarization direction through the stress field, resulting in oscillations. Thus bipedal motion is facilitated by the possibility of oscillation of the polarization direction. This explains why bipedal oscillations are not observed when $e = 0$, since the centrosymmetric actin velocity field lacks polarization altogether.

The travelling kinks observed travelling perpendicular to the average cell direction of motion at the high polarization regime can be understood to some extent, by noting first that a high polarization creates a strong retrograde actin flow v_s in (2.7) that inhibits forward motion (2.10) at the leading edge. The retrograde flow due to polarization inhibits the lamellipodium normal speed V_n by a factor proportional to $e\bar{v} \cdot \boldsymbol{n}$; see (2.7). Hence maximum inhibition occurs when $\boldsymbol{n}$

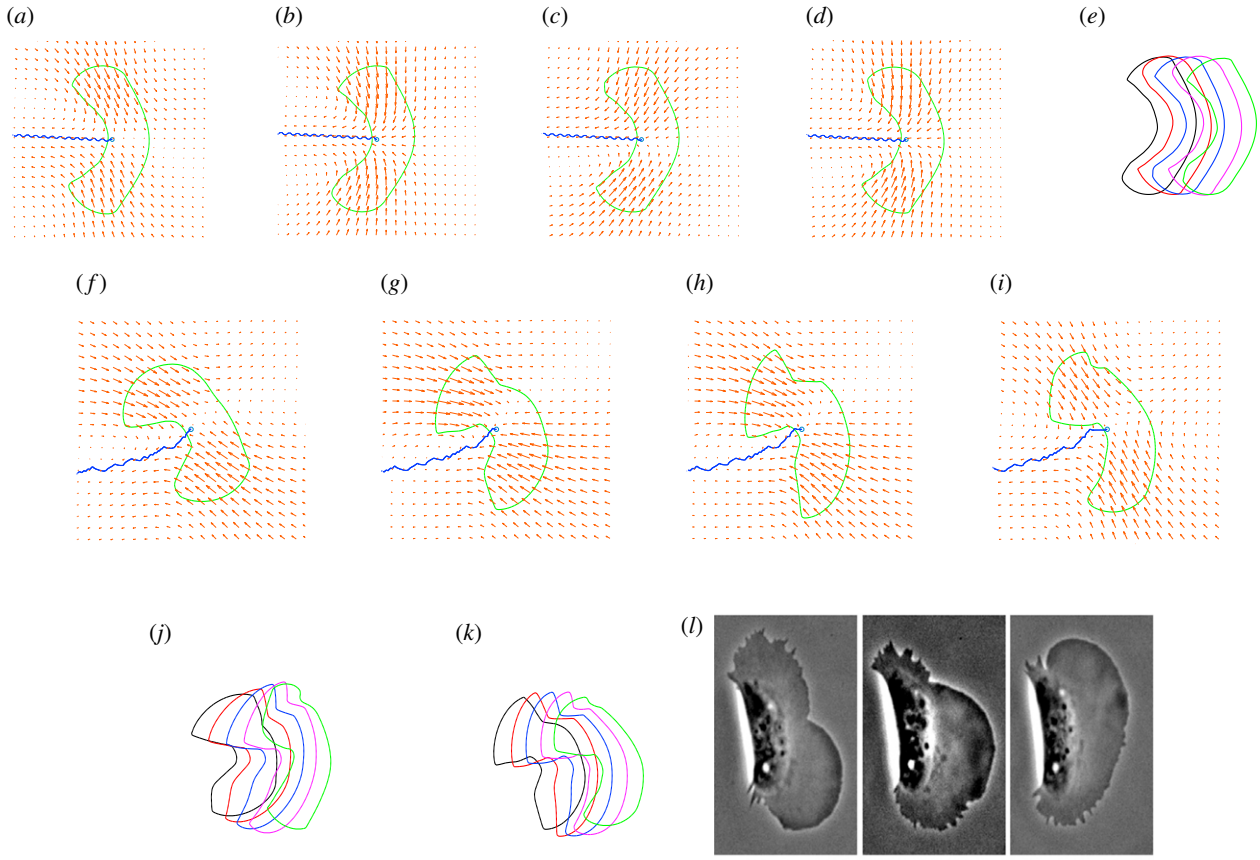

Figure 4. (*a–e*) Intermediate polarization regime: $K = 3$, $e = 3$. Snapshots during a period of bipedal oscillation. In (*a*,*c*), the substrate displacement fields (red arrows) are roughly antisymmetric about the *x*-axis and mirror images to each other. In (*b*,*d*), they are nearly symmetric about the *x*-axis. By contrast, the upper and lower posterior trailing edges are pointed and rounded, respectively in (*b*), and reversed in (*d*) so locomotion is bipedal and the displacement oscillates between symmetry and antisymmetry about the *x*-axis. See also figure 5. Note the rather regular oscillatory centroid trajectory with slight deviation from the *x*-axis (blue curve). (*e*) Overlaid lamellipodium contours, showing upper/lower trailing edges switching between pointed/rounded and rounded/pointed. (*f –l*) High polarization regime: $K = 3$, $e = 11$. (*f –i*) Four successive snapshots illustrating a kink (travelling wave) on the lamellipodium front (green curve) nucleating in (*f*), growing in (*g*) and travelling outward in (*h*) and (*i*). Note the irregular shape and curved, jagged centroid trajectory with large deviation from the *x*-axis (blue curve). (*j*,*k*): Overlaid lamellipodium contours showing two examples of kinks (travelling waves) travelling upwards along the anterior lamellipodium boundary. Analogous sequence of a kink moving upwards from experiments, reproduced from fig. 1A in [43].

is along the direction of motion $\bar{v}$; this agrees with forward velocity decreasing as e increases (figure 3*e*). By contrast, minimal inhibition occurs for $\boldsymbol{n}$ perpendicular to $\bar{v}$, which explains why kinks can propagate nearly perpendicular to the average motion direction.

3.1.4. Substrate displacement and traction prediction

We next compare predicted actin velocity, substrate displacements and tractions to experiments. The velocity field (2.7) in our model, which is prescribed for given parameters, exhibits larger inward flow at the posterior horns of the lamellipodium figure 6*c*) and smaller retrograde flow at the front (right side). This agrees to some extent with observations of [18] shown here in figure 6*b*, although not quantitatively.

The predicted substrate displacement field, figure 6*d* shows some qualitative similarities with measured displacements using traction force microscopy [30], figure 6*e*, in particular, arrows a curve towards the rear as the *x*-axis is approached from the trailing horns in a similar way. In our model, actin velocity is proportional to traction, so figure 6*c* is representative of traction vectors, while figure 6*f* , traction inferred from discrete experimental displacement [30], does not compare so well with figure 6*c*.

3.1.5. Response to external stimuli and tensotaxis

Fibroblasts respond to external forces applied remotely on the elastic substrate by changing shape and direction of motion. When microneedles are used to induce stresses on the substrate, fibroblasts—either the entire cell or a protrusion—tend to move towards tensile stresses and away from compressive stresses [10]. This is known as tensotaxis. While we are unaware of similar experiments on whole keratocytes, we examine whether our model predicts tensotaxis. Lamellipodial fragments that are severed from the keratocyte lamellipodium, and do not contain the nucleus or organelles, behave similar to entire cells [17]. They are disk-shaped when stationary. When pushed by a one-sided external force, they break symmetry, become crescent shaped and start propagating steadily away from the pushing force, even after the latter is removed. While we cannot model the direct application of force onto the cell body, we simulate a situation similar to the experiments of [10]. A force (uniform traction over a disk-shaped area) is applied onto the substrate some distance from the circular stationary lamellipodium fragment, pointing towards it. The force is applied for a short time, then removed. In response, an indentation forms spontaneously, as part of the fragment boundary retreats away from the applied force. This breaks the symmetry of the

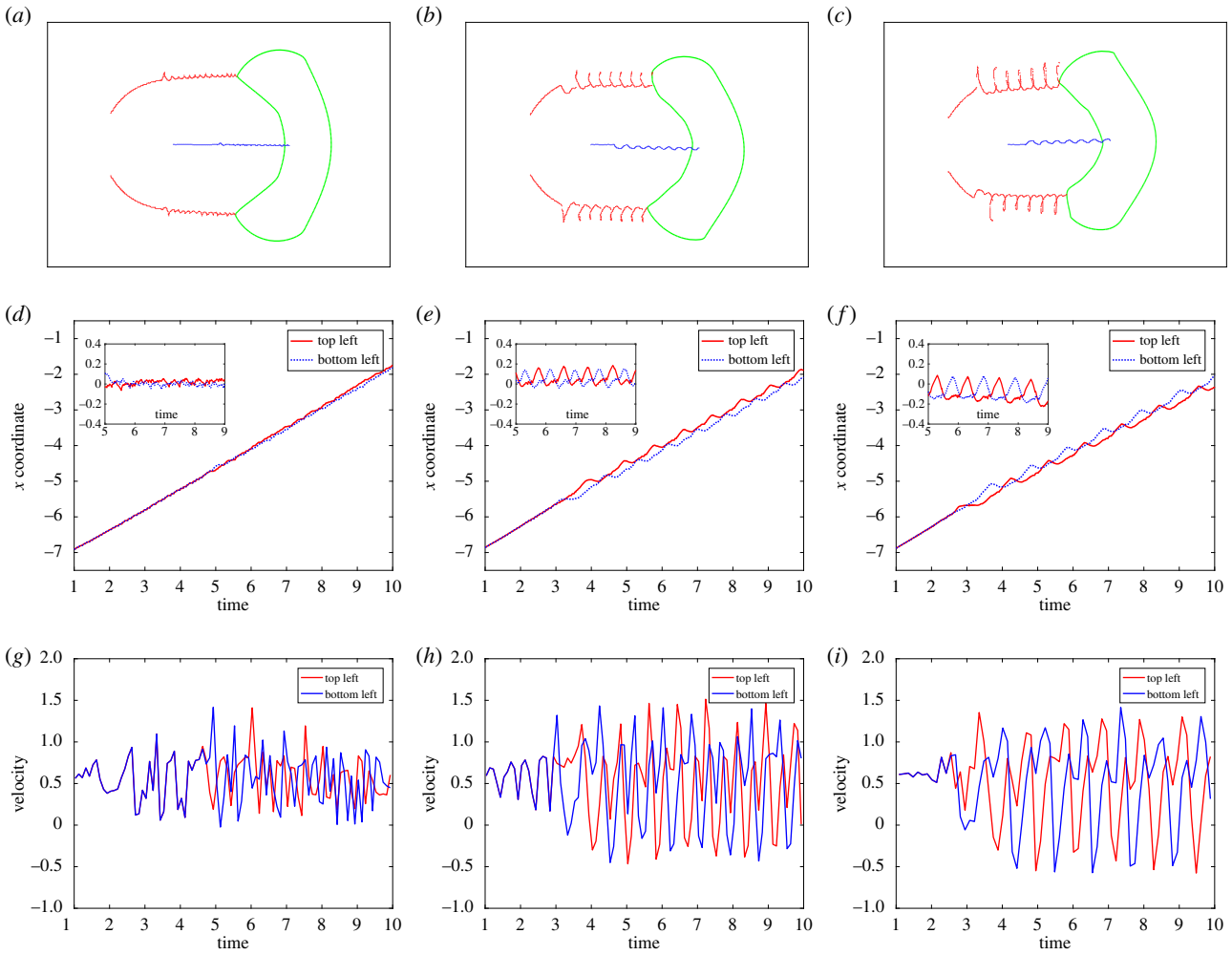

Figure 5. Bipedal oscillatory motion of the two rearmost (trailing) points of the posterior lamellipodium boundary. (*a–c*) Trajectories for $e = 2, 3, 5$, respectively. Red curves: trajectories of trailing points. Blue curve: lamellipodium centroid trajectory. Note intermittent backward motion in (*c*) causing loops in trajectories. (*d–f*) *X*-coordinates of trailing points versus time for $e = 2, 3, 5$, respectively. Red graph: top leftmost point, blue graph: bottom leftmost point. Inserts: deviations of *x*-coordinates from uniform motion with velocity equal to the average velocity (difference from linear fits of *x*-coordinate versus time graphs). (*g–i*) *X*-velocities of trailing points versus time for $e = 2, 3, 5$, respectively. Note alternating (antiphase) top/bottom trailing-point *x*-deviation peaks in (*e*) and (*h*), and velocity peaks in (*h*) and (*i*). Negative velocity peaks in (*h*) and (*i*) indicate intermittent alternating backward motion of trailing points. Computational units in graphs (*d–f*) *x*-unit = 5 µm and *t*-unit =15 s.

fragment, which becomes crescent shaped and starts propagating away from the applied force site; figure 7.

Steady propagation in crescent form continues even though the force has been removed. A similar sequence of events occurs in experiments [17] but due to direct pushing of the fragment instead of the substrate. Instead, here the applied force induces compressive stress between where it is applied and the lamellipodium fragment, which in turn causes the boundary velocity of the cell to become negative in the location closest to the applied force site; thus the symmetry is broken, eventually leading to the crescent shape and steady propagation away from the location of the force, even after the latter ceases to act.

By contrast, when the direction of the applied force is opposite (away from the lamellipodium fragment) tensile stress is generated in front of the fragment, leading to protrusion towards the force site, symmetry breaking, and in some instances, propagation in crescent shape in the direction of the applied force even after the latter is removed; figure 8. This occurs for ellipsoidal fragments with the long axis transversal to the pulling force. Circular fragments tend to elongate in the direction of the pull, then stop after the pulling force is removed. These simulations exhibit tensotaxis: either motion away from higher compressive stress or protrusion and/or motion towards greater tensile stress. This behaviour has similarities with that of fibroblasts [10], although it seems not to have been investigated in the case of keratocytes. More recently [44], relevant behaviour was observed with human epithelial keratinocytes, which are closer to fish epidermal keratocytes than fibroblasts. A needle pulls the substrate behind a locomoting cell and away from it. The cell turns, moves away transversally to the original direction, elongates towards the needle, similar to what happens in the case of a circular fragment, then gradually turns towards the needle. See electronic supplementary material, video SV6 for a simulation capturing various stages of this behaviour qualitatively.

3.1.6. Turning towards stiffer substrates and durotaxis

On a substrate with an interface between regions of different stiffness, cells that assume a crescent morphology similar to keratocytes starting on the softer region, have been observed to follow a curved trajectory, so that they turn towards, and cross into, the stiffer portion of the substrate [45].

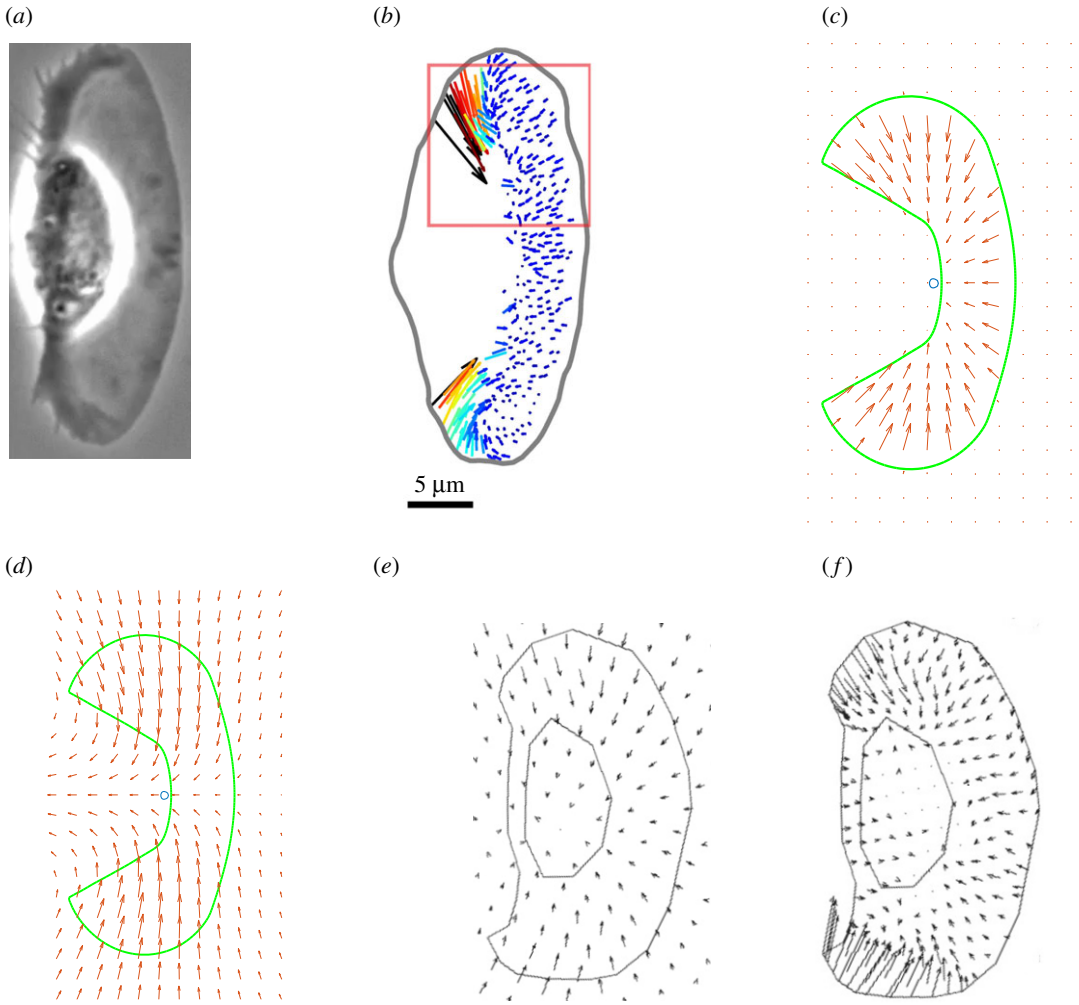

Figure 6. Comparison of lamellipodium shape (*a*) versus (*c*), actin velocity (*b*) versus (*c*), substrate displacement (*d*) versus (*e*) and traction (*f*) versus (*a*) from experiments ((*a*), (*b*), (*e*), (*f*)), and our model (*c*,*d*). (*a*) Motile keratocyte with nearly steady shape and speed (moving to the right) from [18], fig. 1E. (*b*) Measured actin velocity vectors in the lamellipodium (blank region corresponds to the nucleus) [18], fig. 1F. (*c*) Simulation of present model predicts steady propagation of the lamellipodium following the sequence shown in figure 1. Green: steady lamellipodium shape; also shown are actin velocity vectors (red); note large inward flow at the rear and smaller speeds in the front in rough qualitative agreement with (*b*). (*d*) Same as (*c*) but red arrows are substrate displacements. (*e*) Substrate displacement and cell shape from [30], fig. 2a. (*f*) Substrate traction inferred from displacements shown in (*e*) from [30], fig. 2b. The ligament to the left of the nucleus in (*e*,*f*) is not part of the lamellipodium.

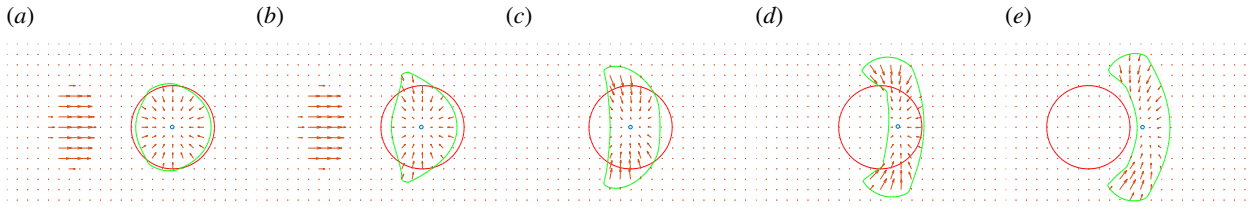

Figure 7. Reverse tensotaxis: model simulation snapshots of a lamellipodium fragment (red: initial fragment position, green: subsequent fragment positions). (*a*) External forces are exerted onto the substrate to the left of the circular fragment (red arrows pointing to the right). (*b*) The fragment starts receding away from the compressive stresses induced by the forces which are about to be removed. (*c*,*d*) The fragment becomes crescent like and starts moving to the right even after the forces are removed. (*e*) It assumes the usual steady shape of a crawling lamellipodium and moves steadily to the right henceforth.

Under zero displacement boundary conditions, the simulation domain boundary becomes equivalent to an interface with a region of infinite stiffness (rigid). We find that cells starting on the central axis of the rectangular symmetric domain typically travel straight along it. However, a cell with initial position closer to the top boundary follows a curving trajectory, while also turning almost rigidly (figure 9), so that it approaches, and eventually contacts, the top boundary; see electronic supplementary material, video SV7. This attraction by a rigid boundary is an instance of durotaxis, and also reproduces the observations of crescent-shaped fibroblasts following a curved trajectory while turning almost rigidly with slight shape change [19].

By contrast, traction-free boundary conditions make the boundary behave like the interface with a softer material, in the limit of zero stiffness. Repeating the previous simulation with traction free conditions makes the cell turn away from the boundary towards the centreline along the x-axis, repelled

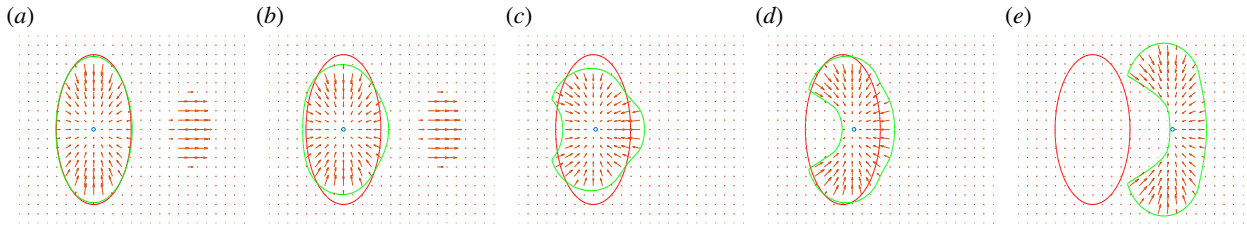

Figure 8. Tensotaxis: model simulation snapshots of a lamellipodium fragment (red: initial fragment position, green: subsequent fragment positions). (*a*) External forces are exerted onto the substrate to the right of the elliptical fragment (red arrows pointing to the right). (*b*) The fragment starts protruding towards the tensile stresses to its right induced by the forces (which are about to be removed). (*c*,*d*) The fragment becomes crescent like and starts moving to the right even after the forces are removed. (*e*) It assumes the usual steady shape of a crawling lamellipodium and moves steadily to the right henceforth.

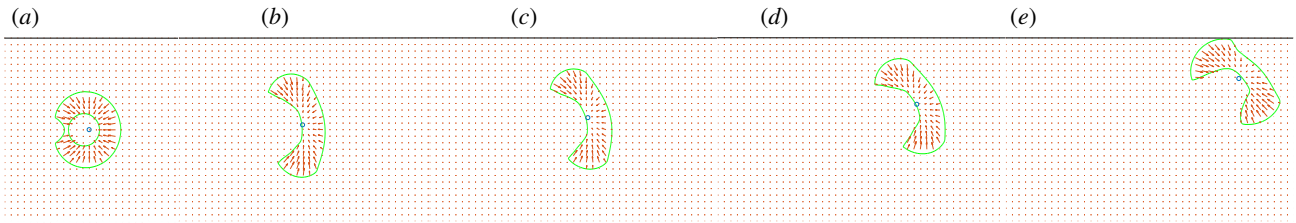

Figure 9. Durotaxis: snapshots of a keratocyte (model simulation; green: lamellipodium, red: actin velocity vectors) near a rigid boundary (top) starting to move to the right as in figure 1*b*, then turning towards a rigid boundary (black line). The shape is slightly distorted as the keratocyte turns, and symmetry about the instantaneous direction of motion is perturbed. Contact of the lamellipodium with the rigid boundary occurs at (*e*).

by the interface with a much softer substrate. See electronic supplementary material, video SV8.

How can a cell sense an interface with a stiffer region at a distance? Our model provides insight into the mechanism responsible for the attraction of cells by a rigid boundary. Cells exert contractile forces onto the substrate. In the vicinity of a rigid boundary, this causes tensile stresses that are highest in the ligament between the boundary and the cell. These tensile stresses are sensed by the cell, which tends to protrude in their direction in accordance with the evolution law. The closer the cell approaches the boundary, the higher this stress becomes; this causes acceleration and the result is a trajectory that curves towards the stiff boundary. This strongly suggests that keratocytes and fibroblasts exert contractile forces in order to probe their surroundings by sensing inhomogeneities in the stress field they themselves generate. In this case, the inhomogeneity is caused by the vicinity of a stiff interface.

4. Conclusions

We have constructed a minimal model for the evolution of fish epidermal keratocytes based on an active mechanosensing hypothesis: we posit that these cells sense the stress field that they themselves actively generate in the substrate, and evolve accordingly, by locally protruding in areas of tension and contracting in areas of compression.

Most previous theoretical models concentrate on the processes inside the cell, such as actin–myosin interaction. By contrast, our model focuses on the mechanical interaction between the lamellipodium and substrate. The model of the cell itself is minimal and consists of an actin velocity field with central symmetry inside an evolving curve representing the lamellipodium boundary. The centripetally flowing actin exerts contractile tractions onto the elastic substrate. The resulting substrate stress depends on the shape of the lamellipodium boundary. At the same time, this stress enters the evolution law at each point of the lamellipodium boundary curve.

In its non-dimensional form, the model involves two coupled partial differential equations and just four independent parameters. The model predicts multiple types of observed behaviour of keratocytes on elastic substrates for the same parameter set. The parameters used are consistent with experiment-based estimates. The well-known crescent shape, characteristic of keratocytes in steady locomotion, emerges through symmetry-breaking bifurcation and a topological change from the annulus-shaped lamellipodium typical of stationary keratocytes, as observed experimentally [18].

It is by now well understood that symmetry breaking is necessary for locomotion, e.g. [55]. In previous models, this was brought about by internal processes of the cell, governing spatial concentrations of actin, myosin and adhesion strength via additional partial differential equations [21–24,31,55]. Here, we identify a new symmetry breaking mechanism: a feedback loop due to mechanosensitive coupling between the lamellipodium shape and substrate stress. Indeed, perturbing the radial symmetry of the static cell shape breaks the symmetry of the substrate stress field, which induces asymmetry of the polymerization velocity (protrusion rate), which in turn amplifies asymmetric polarized shape evolution, closing the feedback loop, even in the presence of a radial, non-polar actin flow. It is likely that this mechanism is complementary to internal actomyosin/adhesion mechanisms, however, our results indicate that it is important in processes involving substrate mechanics, notably tensotaxis and durotaxis.

When the model is generalized to include actin velocity polarization in the direction of motion, further symmetry breaking occurs, leading to two additional types of complex locomotion behaviour observed in experiments. For high enough polarization, reflection symmetry of the lamellipodium is lost and steady motion of the crescent bifurcates

into oscillatory bipedal asymmetric locomotion. Here, actin velocity polarization provides another mechanism for symmetry breaking. The polarization direction is an additional degree of freedom that can oscillate out of phase with the lamellipodium. Further increases of the polarization parameter yield more irregular, slower oscillations with increased distortion of the lamellipodium shape, in the form of alternating travelling waves (kinks) moving along the leading lamellipodium edge transversal to the average motion. Keratocytes exhibit both phenomena [31,42]. The three main types of locomotion, steady, bipedal/oscillatory and wavelike, are due to a series of symmetry breaking bifurcations starting from the radially symmetric stationary annular lamellipodium.

When microneedles are used to induce stresses in the substrate, fibroblasts tend to move towards tensile stresses and away from compressive stresses [10,17,44]. In our simulations, a localized traction force on the substrate, some distance away from the cell, creates either a compressive or tensile stress between the force and the cell (when pointing towards or away from the cell, respectively). The cell either moves away from a force pointing towards it, or protrudes towards a force in the opposite direction. This is an example of tensotaxis. Unfortunately, such experiments seem not to have been performed with fish keratocytes, but recently with human keratinocytes [44]; our model captures essential aspects of these experiments.

Our model exhibits a form of durotaxis, whereby simulated cells are attracted by the closest rigid boundary and curve their trajectories towards it, similar to observed motion of crescent-shaped cells towards interfaces with stiffer regions [45]. The model allows us to identify the mechanism underlying this attraction as cell-induced tensile stress, which is highest in the region between the cell and the closest boundary, leading to protrusion towards the latter.

We believe that the present model is the first to explain multiple types of keratocyte locomoting behaviour, by identifying new mechanisms of symmetry breaking, facilitated by active mechanosensing. Despite a combination of non-local and nonlinear effects, the model is comparatively simple; hopefully, future bifurcation and post-bifurcation analysis will provide additional insights into the underlying mechanisms responsible for complex observed behaviour such as bipedal oscillations and travelling waves.

The model also provides insight into phenomena such as tensotaxis and durotaxis, more commonly observed with fibroblasts and other cells. To test the validity of the active mechanosensing hypothesis further, it would be interesting to perform experiments analogous to [10,17,44,45], but with fish keratocytes instead of fibroblasts, on substrates where remote forces are exerted by microneedle, or where substrate stiffness varies with position, either gradually or discontinuously. It will be especially instructive to determine in what ways mechanosensing affects differences in morphology and locomotion between keratocytes and fibroblasts, or other cells known to be mechanosensitive.

Data accessibility. The numerical code used in the simulations reported herein is available at: https://github.com/CellEvolution/cellevolution/tree/master/KeratocyteCode.

Authors' contributions. Z.Z. wrote the numerical code and ran the simulations, P.R. developed the model, all authors analysed and discussed the model and results. T.Y.H. and G.R. critically revised the manuscript. All authors gave final approval for publication and agree to be held accountable for the work performed therein.

Competing interests. We declare we have no competing interest.

Funding. The research of Z.Z. was supported in part by the Hong Kong RGC grants (Projects 27300616, 17300817 and 17300318), National Natural Science Foundation of China (Project 11601457), and Seed Funding Programme for Basic Research (HKU). Z.Z. thanks the support and hospitality of T.Y.H. when he was a postdoctoral scholar at Caltech. The research of P.R. was partially supported by the EU Horizon 2020 Research and Innovation Program under the Marie Sklodowska-Curie project modcompshock.eu, agreement no. 642768. The research of T.Y.H. was supported in part by NSF grant nos. DMS-1907977 and DMS-1912654. G.R. acknowledges the support of the National Science Foundation (DMR no. 0520565) through the Center for Science and Engineering of Materials at the California Institute of Technology.

References

1. Harris AK, Wild P, Stopak D. 1980 Silicone rubber substrata: a new wrinkle in the study of cell locomotion. *Science* **208**, 177–179. (doi:10.1126/science.6987736)
2. Beningo KA, Wang Y-L. 2002 Flexible substrata for the detection of cellular traction forces. *Trends Cell Biol.* **12**, 79–84. (doi:10.1016/S0962-8924(01)02205-X)
3. Burton K, Park JH, Taylor DL. 1999 Keratocytes generate traction forces in two phases. *Mol. Biol. Cell* **10**, 3745–3769. (doi:10.1091/mbc.10.11.3745)
4. Burton K, Taylor DL. 1997 Traction forces of cytokinesis measured with optically modified elastic substrata. *Nature* **385**, 450. (doi:10.1038/385450a0)
5. De R, Zemel A, Safran SA. 2008 Do cells sense stress or strain? Measurement of cellular orientation can provide a clue. *Biophys. J.* **94**, L29–L31. (doi:10.1529/biophysj.107.126060)
6. Schwarz US, Bischofs IB. 2005 Physical determinants of cell organization in soft media. *Med. Eng. Phys.* **27**, 763–772. (doi:10.1016/j.medengphy.2005.04.007)
7. Moore SW, Roca-Cusachs P, Sheetz MP. 2010 Stretchy proteins on stretchy substrates: the important elements of integrin-mediated rigidity sensing. *Dev. Cell* **19**, 194–206. (doi:10.1016/j.devcel.2010.07.018)
8. Chen B, Ji B, Gao H. 2015 Modeling active mechanosensing in cell–matrix interactions. *Annu. Rev. Biophys.* **44**, 1–32. (doi:10.1146/annurev-biophys-051013-023102)
9. Beloussov LV, Louchinskaia NN, Stein AA. 2000 Tension-dependent collective cell movements in the early gastrula ectoderm of *Xenopus laevis* embryos. *Dev. Genes Evol.* **210**, 92–104. (doi:10.1007/s004270050015)
10. Lo C-M, Wang H-B, Dembo M, Wang YI. 2000 Cell movement is guided by the rigidity of the substrate. *Biophys. J.* **79**, 144–152. (doi:10.1016/S0006-3495(00)76279-5)
11. Wong VW, Longaker MT, Gurtner GC. 2012 Soft tissue mechanotransduction in wound healing and fibrosis. *Semin. Cell Dev. Biol.* **23**, 981–986. (doi:10.1016/j.semcdb.2012.09.010)
12. Discher DE, Smith L, Cho S, Colasurdo M, García AJ, Safran S. 2017 Matrix mechanosensing: from scaling concepts in 'omics data to mechanisms in the nucleus, regeneration, and cancer. *Annu. Rev. Biophys.* **46**, 295–315. (doi:10.1146/annurev-biophys-062215-011206)
13. Ben-Yaakov D, Golkov R, Shokef Y, Safran SA. 2015 Response of adherent cells to mechanical perturbations of the surrounding matrix. *Soft Matter* **11**, 1412–1424. (doi:10.1039/C4SM01817F)
14. Golkov R, Shokef Y. 2017 Shape regulation generates elastic interaction between living cells. *New J. Phys.* **19**, 063011. (doi:10.1088/1367-2630/aa70ef)
15. Cox BN, Snead ML. 2016 Cells as strain-cued automata. *J. Mech. Phys. Solids* **87**, 177–226. (doi:10.1016/j.jmps.2015.11.002)

16. Janmey PA, Winer JP, Murray ME, Wen Q. 2009 The hard life of soft cells. *Cytoskeleton* **66**, 597–605. (doi:10.1002/cm.20382)
17. Verkhovsky AB, Svitkina TM, Borisy GG. 1999 Self-polarization and directional motility of cytoplasm. *Curr. Biol.* **9**, 11–S1. (doi:10.1016/S0960-9822(99)80042-6)
18. Yam PT, Wilson CA, Ji L, Hebert B, Barnhart EL, Dye NA, Wiseman PW, Danuser G, Theriot JA. 2007 Actin–myosin network reorganization breaks symmetry at the cell rear to spontaneously initiate polarized cell motility. *J. Cell Biol.* **178**, 1207–1221. (doi:10.1083/jcb.200706012)
19. Oliver T, Dembo M, Jacobson K. 1999 Separation of propulsive and adhesive traction stresses in locomoting keratocytes. *J. Cell Biol.* **145**, 589–604. (doi:10.1083/jcb.145.3.589)
20. Riaz M, Versaevel M, Mohammed D, Glinel K, Gabriele S. 2016 Persistence of fan-shaped keratocytes is a matrix-rigidity-dependent mechanism that requires α5β1 integrin engagement. *Sci. Rep.* **6**, 34141. (doi:10.1038/srep34141)
21. Keren K, Pincus Z, Allen GM, Barnhart EL, Marriott G, Mogilner A, Theriot JA. 2008 Mechanism of shape determination in motile cells. *Nature* **453**, 475. (doi:10.1038/nature06952)
22. Rubinstein B, Fournier MF, Jacobson K, Verkhovsky AB, Mogilner A. 2009 Actin–myosin viscoelastic flow in the keratocyte lamellipod. *Biophys. J.* **97**, 1853–1863. (doi:10.1016/j.bpj.2009.07.020)
23. Wolgemuth CW, Stajic J, Mogilner A. 2011 Redundant mechanisms for stable cell locomotion revealed by minimal models. *Biophys. J.* **101**, 545–553. (doi:10.1016/j.bpj.2011.06.032)
24. Shao D, Levine H, Rappel W-J. 2012 Coupling actin flow, adhesion, and morphology in a computational cell motility model. *Proc. Natl Acad. Sci. USA* **109**, 6851–6856. (doi:10.1073/pnas.1203252109)
25. Löber J, Ziebert F, Aranson IS. 2014 Modeling crawling cell movement on soft engineered substrates. *Soft Matter* **10**, 1365–1373. (doi:10.1039/C3SM51597D)
26. Ziebert F, Aranson IS. 2016 Computational approaches to substrate-based cell motility. *npj Comput. Mater.* **2**, 16019. (doi:10.1038/npjcompumats.2016.19)
27. Kim M-C, Silberberg YR, Abeyaratne R, Kamm RD, Asada HH. 2018 Computational modeling of three-dimensional ECM-rigidity sensing to guide directed cell migration. *Proc. Natl Acad. Sci. USA* **115**, E390–E399. (doi:10.1073/pnas.1717230115)
28. Sokolnikoff IS. 1956 *Mathematical theory of elasticity*. New York, NY: Mcgraw-Hill Book Company.
29. Dembo M, Oliver T, Ishihara A, Jacobson K. 1996 Imaging the traction stresses exerted by locomoting cells with the elastic substratum method. *Biophys. J.* **70**, 2008–2022. (doi:10.1016/S0006-3495(96)79767-9)
30. Doyle A, Marganski W, Lee J. 2004 Calcium transients induce spatially coordinated increases in traction force during the movement of fish keratocytes. *J. Cell Sci.* **117**, 2203–2214. (doi:10.1242/jcs.01087)
31. Barnhart EL, Lee K-C, Keren K, Mogilner A, Theriot JA. 2011 An adhesion-dependent switch between mechanisms that determine motile cell shape. *PLoS Biol.* **9**, e1001059. (doi:10.1371/journal.pbio.1001059)
32. Galkin VE, Orlova A, Egelman EH. 2012 Actin filaments as tension sensors. *Curr. Biol.* **22**, R96–R101. (doi:10.1016/j.cub.2011.12.010)
33. Romet-Lemonne G, Jégou A. 2013 Mechanotransduction down to individual actin filaments. *Eur. J. Cell Biol.* **92**, 333–338. (doi:10.1016/j.ejcb.2013.10.011)
34. Plotnikov SV, Waterman CM. 2013 Guiding cell migration by tugging. *Curr. Opin. Cell Biol.* **25**, 619–626. (doi:10.1016/j.ceb.2013.06.003)
35. Jégou A, Carlier M-F, Romet-Lemonne G. 2013 Formin mDia1 senses and generates mechanical forces on actin filaments. *Nat. Commun.* **4**, 1–7. (doi:10.1038/ncomms2888)
36. Higashida C, Kiuchi T, Akiba Y, Mizuno H, Maruoka M, Narumiya S, Mizuno K, Watanabe N. 2013 F- and g-actin homeostasis regulates mechanosensitive actin nucleation by formins. *Nat. Cell Biol.* **15**, 395–405. (doi:10.1038/ncb2693)
37. Zhong Y, Ji B. 2014 How do cells produce and regulate the driving force in the process of migration? *Eur. Phys. J. Spec. Top.* **223**, 1373–1390. (doi:10.1140/epjst/e2014-02196-8)
38. Osher S, Sethian JA. 1988 Fronts propagating with curvature-dependent speed: algorithms based on Hamilton–Jacobi formulations. *J. Comput. Phys.* **79**, 12–49. (doi:10.1016/0021-9991(88)90002-2)
39. Chang YC, Hou TY, Merriman B, Osher S. 1996 A level set formulation of eulerian interface capturing methods for incompressible fluid flows. *J. Comput. Phys.* **124**, 449–464. (doi:10.1006/jcph.1996.0072)
40. Sethian JA. 1999 *Level set methods and fast marching methods: evolving interfaces in computational geometry, fluid mechanics, computer vision, and materials science*, vol. 3. Cambridge, UK: Cambridge University Press.
41. Wolgemuth CW, Zajac M. 2010 The moving boundary node method: a level set-based, finite volume algorithm with applications to cell motility. *J. Comput. Phys.* **229**, 7287–7308. (doi:10.1016/j.jcp.2010.06.014)
42. Barnhart EL, Allen GM, Jülicher F, Theriot JA. 2010 Bipedal locomotion in crawling cells. *Biophys. J.* **98**, 933–942. (doi:10.1016/j.bpj.2009.10.058)
43. Barnhart EL, Allard J, Lou SS, Theriot JA, Mogilner A. 2017 Adhesion-dependent wave generation in crawling cells. *Curr. Biol.* **27**, 27–38. (doi:10.1016/j.cub.2016.11.011)
44. Zarkoob H, Chinnathambi S, Selby JC, Sander EA. 2018 Substrate deformations induce directed keratinocyte migration. *J. R. Soc. Interface* **15**, 20180133. (doi:10.1098/rsif.2018.0133)
45. Wormer DB, Davis KA, Henderson JH, Turner CE. 2014 The focal adhesion-localized CdGAP regulates matrix rigidity sensing and durotaxis. *PLoS ONE* **9**, e91815. (doi:10.1371/journal.pone.0091815)
46. Schwarz US, Safran SA. 2013 Physics of adherent cells. *Rev. Mod. Phys.* **85**, 1327. (doi:10.1103/RevModPhys.85.1327)
47. Lemmon CA, Romer LH. 2010 A predictive model of cell traction forces based on cell geometry. *Biophys. J.* **99**, L78–L80. (doi:10.1016/j.bpj.2010.09.024)
48. Rape AD, Guo W-h., Wang Y-l. 2011 The regulation of traction force in relation to cell shape and focal adhesions. *Biomaterials* **32**, 2043–2051. (doi:10.1016/j.biomaterials.2010.11.044)
49. Moure A, Gomez H. 2020 Dual role of the nucleus in cell migration on planar substrates. *Biomech. Model. Mechanobiol.* 1–18. (doi:10.1007/s10237-019-01283-6)
50. Gao Z, Gao Y. 2016 Why do receptor–ligand bonds in cell adhesion cluster into discrete focal-adhesion sites? *J. Mech. Phys. Solids* **95**, 557–574. (doi:10.1016/j.jmps.2016.05.012)
51. Mogilner A, Keren K. 2009 The shape of motile cells. *Curr. Biol.* **19**, R762–R771. (doi:10.1016/j.cub.2009.06.053)
52. Blanch-Mercader C, Casademunt J. 2013 Spontaneous motility of actin lamellar fragments. *Phys. Rev. Lett.* **110**, 078102. (doi:10.1103/PhysRevLett.110.078102)
53. Lin S-L, Yang J-C, Ho K-N, Wang C-H, Yeh C-W, Huang H-M. 2009 Effects of compressive residual stress on the morphologic changes of fibroblasts. *Med. Biol. Eng. Comput.* **47**, 1273. (doi:10.1007/s11517-009-0512-6)
54. Gurtin ME. 1973 The linear theory of elasticity. In *Linear theories of elasticity and thermoelasticity*, pp. 1–295. New York, NY: Springer.
55. Barnhart E, Lee K-C, Allen GM, Theriot JA, Mogilner A. 2015 Balance between cell–substrate adhesion and myosin contraction determines the frequency of motility initiation in fish keratocytes. *Proc. Natl Acad. Sci. USA* **112**, 5045–5050 (doi:10.1073/pnas.1417257112)